On process-step parallel computability and linear superposition of mechanical responses in additive manufacturing process simulation

Munro, Dirk; Ayas, Can; Langelaar, Matthijs; van Keulen, Fred

DOI
10.1016/j.addma.2019.06.023

Publication date
2019

Document Version
Final published version

Published in
Additive Manufacturing

Citation (APA)
Munro, D., Ayas, C., Langelaar, M., & van Keulen, F. (2019). On process-step parallel computability and linear superposition of mechanical responses in additive manufacturing process simulation. *Additive Manufacturing* , *28*, 738-749. https://doi.org/10.1016/j.addma.2019.06.023

Additive Manufacturing 28 (2019) 738–749

Contents lists available at ScienceDirect

Additive Manufacturing

journal homepage: www.elsevier.com/locate/addma

On process-step parallel computability and linear superposition of mechanical responses in additive manufacturing process simulation

Dirk Munro*, Can Ayas, Matthijs Langelaar, Fred van Keulen

Delft University of Technology, Faculty of Precision and Microsystems Engineering, Department of Mechanical, Maritime and Materials Engineering, Mekelweg 2, 2628 CD Delft, The Netherlands

ARTICLE INFO

Keywords:
Additive manufacturing
Macroscale mechanical modeling
Residual stress
Distortion
Parallel computation

ABSTRACT

We study linearity assumptions in the transient macroscale mechanical aspect of additive manufacturing (AM) process simulation. Linearity assumptions are often resorted to in combination with calibrated inelastic deformation components to arrive at computationally tractable yet reasonably accurate AM process models. We point out that linearity assumptions permit the independent computation of the response increment in each step of the AM process, and the total mechanical response is the superposition of all the process-step increments. In effect, process-step increments are computed with respect to the stress-free reference configuration in each step. The implication is that the mechanical response increment in each linearised AM process step may be computed in parallel. Trivial process-step-wise parallel computability breaks down, however, if nonlinearity (*i.e.* geometric or material) is modelled. In our investigation the influence of geometric nonlinearity on part distortion is small (but this is of course part-geometry specific), and more realistic stresses are obtained by imposing a nonlinear elastoplastic material law after the parallel computation and superposition of the linear AM response increments. It is demonstrated that simulation wall-clock time is reduced by exploiting process-step parallel computability in the linear regime. Moreover, numerical experiments suggest that process-step parallelization scales better (in wall-clock time) than conventional parallelization in the sequential computation of each response increment.

1. Introduction

Descriptions of additive manufacturing (AM) processes are often dedicated to the notion that the parts and structures which are produced, arise in a layer-by-layer fashion [1–4]. In principle, sufficient control of AM processes (*e.g.* material properties, deposition order, energy input) permit the production of near net shape parts and structures with tailored microstructural features [5,6]. Due to the minimal (re)tooling costs associated with the production of a diverse range of structural geometries, AM processes are seen to have novel implications with respect to the usual economies of scope and of scale [7–10]. From a design-engineer's point of view, the main advantage of AM is the liberty afforded in the (quick) realization of complex and efficient parts and structures—by exploiting, potentially, computational design-optimization techniques—with less assembly time and more flexible functional integrations [11,12].

AM manufacturing techniques operate on a range of materials. Herein we focus on metal AM, particularly notorious for defects, dimensional inaccuracy, and difficulties in micro-structural control. Megahed et al. [13] classify existing metal AM processes based on the manner in which the material is deposited prior to fusion, referring to powder-bed, blown-powder, and wire-feed processes. The predominant metal AM technology is selective laser melting (SLM), a powder bed process [14–18]. In general, metal AM technology is characterized by a localized heat (energy) input directed in such a way as to (at least partially) melt and fuse the deposited material with the existing structure. The phase changes and temperature gradients cause deformation, stress, and part distortion [13,15,16]. The properties of the deposited material and the action by which it is bonded or fused—in terms of thermofluid effects—determine the mechanical properties of the consequential structure [14,19–21]. Megahed et al. [13] highlight the multiphysics character of the process, and the fact that the small time and length scales associated with the heat source have to be accounted for (relative to the macroscopic scale of the part). In varying degrees, the aforementioned phenomena contribute to undesirable surface finishes and material properties, dimensional inaccuracy, degraded performance, and premature failure of the part (in service). In short, violation of design tolerances. In the extreme, the part or structure may distort excessively and/or fail during the build, and cause failure (typically obstruction) of the AM machine [22,23].

* Corresponding author.
E-mail address: dirkmunro8@gmail.com (D. Munro).

https://doi.org/10.1016/j.addma.2019.06.023
Received 31 July 2018; Received in revised form 12 February 2019; Accepted 24 June 2019
Available online 26 June 2019
2214-8604/

The complexities which *per se* accompany the strengths of AM implicate computational simulation in an attempt to predict, control, and potentially exploit the (seemingly undesirable) side-effects of the process [7]. If computational simulation is not available, costly and time-consuming physical trial-and-error experiments have to be resorted to [24–26]. Simulation technology permits a designer to compensate *a priori* for the process responses with design modifications [27], design-optimization of the part with respect to the process [28], or optimization of the process itself as a function of the process parameters [16].

Due to the predominance of thermomechanical effects, one branch of fast AM process simulation is focused on the efficient calculation of the thermal history of the build. Depending on the particular thermo-mechanical coupling—invariably one-way—the temperature histories form the input to a macroscale mechanical analysis in order to predict residual stress fields and part distortion. Zeng and co-workers [29,30] employ a dynamically meshed finite element (FE) model to reduce the number of degrees of freedom (and thereby reduce the computational burden) [29,30]. Yang et al. [31] also manage to decouple (to some extent) the FE discretization from the accuracy of the thermal history calculation. To reduce computation time, cheap analytical solutions of the steep thermal gradients in and around the heat source are superimposed on a relatively course FE mesh [31]. Both approaches [29–31] permit the simulation of specific scanning paths and patterns in SLM. However, Heigel et al. [32] point out that a measurement-based convection model may be necessary in order to predict accurate thermal histories in metal AM. Moreover, Ghosh and Choi [19] advocate modelling of the phase transformation kinetics in laser-aided metal AM in order to calculate accurate residual stress distributions. Similarly, Mukherjee et al. [33] propose a transient heat transfer and fluid-flow SLM model—in order to simulate, in particular, the convective thermal interactions associated with the meltpool—combined with a thermo-mechanical analysis to determine accurate macroscale stress and distortion. Yet, the computation of only the transient thermofluid fields in the equivalent of a 5-layer build (using an adaptive FE mesh), requires about 5 h of wall-clock time on a contemporary hardware platform (the simulation requires about 30 h using a conventional 'brute-force' FE mesh) [34].

With an eye on the computational burden, Neugebauer and co-workers [27,35] develop a hierarchical multiscale computational procedure (for SLM) whereby a generic microscale heat source model is mapped to a layer-wise hatching model, serving as input to a 'lumped' mechanical layer equivalent (MLE) analysis. Li et al. [36] adopt much the same approach. To the end of fast computation of the mechanical process responses, the sub-macroscale models are used to predetermine a so-called *inherent* strain, accompanying each layer in the MLE. A similar technique is used successfully in welding distortion prediction [37]. Reportedly, calculation time is reduced by two or more orders of magnitude if the sub-macroscale phenomena are predetermined and averaged ('lumped') in this way. Zaeh and Branner [23] also lump several layers (in SLM) in order to reduce computation time to reasonable levels. Alvarez, San Sebastian, Setien and co-workers [38,39] refer to the MLE as the inherent shrinkage method (originally developed for multi-pass welding processes), and employ calibrated anisotropic inherent strain fields to model different hatching patterns in SLM [40].

In this paper we adopt the philosophy outlined directly above, and follow the conventional inherent strain approach. That is to say, to the end of fast computation of the mechanical AM process responses, the macroscale manifestation of the phase-changes and thermal gradients are predetermined and applied as an inelastic deformation field, within a FE-based representation of a growing structural configuration. Throughout, we highlight and explore the fact that standard linearity assumptions permit the independent computation of the mechanical response increment in each step of the AM process simulation. Section 2 departs with an outline of the relevant structural behaviour from a computational mechanics point of view, followed by the formulation of the AM process model itself. Section 3 contains discussions on implementation aspects, numerical demonstrations, and experiments, devised to shed light on the accuracy and the speed of the linearised AM process simulation. Section 4 provides a final discussion and conclusions.

2. The AM process model

2.1. Elastoplastic structural behaviour under geometric linearity assumptions

We choose to study structural configurations by computational means, using the well-known finite element (FE) method. To avoid cumbersome descriptions of the details of the FE's, we employ a generalized description. To this end, we introduce an array of generalized deformation components $\boldsymbol{\varepsilon}$ which describe the deformation of the structure. The total number and composition of deformation components is determined by the discretization and types of elements (cumbersome details of which we can thus avoid). In matrix notation, the array of generalized deformation components is $\boldsymbol{\varepsilon}^T = (\boldsymbol{\varepsilon}_1^T, \boldsymbol{\varepsilon}_2^T, \ldots)$, in which $\boldsymbol{\varepsilon}_e$ is a column representing the generalized deformations of element e. Similarly, we have energetically conjugate generalized stresses $\boldsymbol{\sigma}$ and $\boldsymbol{\sigma}_e$, such that the inner products $\boldsymbol{\sigma}_e \cdot \delta\boldsymbol{\varepsilon}_e$ and $\boldsymbol{\sigma} \cdot \delta\boldsymbol{\varepsilon}$ yield the (correct) internal virtual work at element—and system-level respectively. For example, consider a standard FE representation of a continuum body, with $\mathbf{S}_e$ the second Piola-Kirchhoff stress tensor and $\mathbf{E}_e$ the Green-Lagrange strain tensor—see, for example, Holzapfel [41]—associated with element e. Element e is demarcated by a volume V_e (in the reference configuration), with the relation

$$\int_{V_e} \mathbf{S}_e : \delta\mathbf{E}_e \, \mathrm{d}V = \boldsymbol{\sigma}_e \cdot \delta\boldsymbol{\varepsilon}_e, \tag{1}$$

taken to hold. Furthermore, $\mathbf{u}$ and $\mathbf{f}$ are the generalized nodal degrees of freedom (dofs) and the work equivalent external nodal loads. Static equilibrium is inferred with the Principle of Virtual Work, which states that

$$\boldsymbol{\sigma} \cdot \delta\boldsymbol{\varepsilon} = \mathbf{f} \cdot \delta\mathbf{u}, \tag{2}$$

for all kinematically admissible variations, $\delta\mathbf{u}$. In reality, the generalized deformations are related to the dofs by

$$\boldsymbol{\varepsilon} = \boldsymbol{\varepsilon}[\mathbf{u}], \tag{3}$$

in a nonlinear manner, and variations follow as

$$\delta\boldsymbol{\varepsilon}_e = \mathbf{D}_e[\mathbf{u}_e]\delta\mathbf{u}_e, \quad \delta\boldsymbol{\varepsilon} = \mathbf{D}[\mathbf{u}]\delta\mathbf{u}, \tag{4}$$

on element—and system-level, respectively; $\mathbf{D}_e$ and $\mathbf{D}$ being the deformation-dof differentiation matrices, which follow from the operation $\frac{\partial \varepsilon_i}{\partial u_j}[\mathbf{u}]$; $\mathbf{u}_e$ are the nodal dofs associated with element e. Square brackets $[\cdot]$ denote functional dependency ('evaluated at'). The functional dependency notation $[\cdot]$ will be used and dropped freely to indicate the nature of a particular quantity at a particular point in our description. Geometric linearity assumptions (small strains and rotations) manifest in constant differentiation matrices

$$\boldsymbol{\varepsilon}_e[\mathbf{u}_e] = \mathbf{D}_e[\mathbf{0}]\mathbf{u}_e, \quad \boldsymbol{\varepsilon}[\mathbf{u}] = \mathbf{D}[\mathbf{0}]\mathbf{u}, \tag{5}$$

with respect to the dofs $\mathbf{u}$. That is, under geometric linearity assumptions, $\mathbf{D}$ and $\mathbf{D}_e$ are evaluated at the reference configuration $\mathbf{u} = \mathbf{0}$, irrespective of the current (computed) state of the configuration.

The generalized stresses $\boldsymbol{\sigma}$ are related to the generalized deformations $\boldsymbol{\varepsilon}$ by a material model. In the linear regime, stress components are related to the deformations with a generalized form of Hooke's law. In the presence of inelastic deformations, a material law is represented by an operation on the elastic part of the deformation components, at element—and system-level

$$\boldsymbol{\sigma}_e = \mathbf{S}_e(\boldsymbol{\varepsilon}_e[\mathbf{u}_e] - \boldsymbol{\varepsilon}_e^\star), \quad \boldsymbol{\sigma} = \mathbf{S}(\boldsymbol{\varepsilon}[\mathbf{u}] - \boldsymbol{\varepsilon}^\star) \tag{6}$$

respectively, with $\mathbf{S}_e$ and $\mathbf{S}$ generic elasticity matrices. As is common, it is assumed that the total deformation $\boldsymbol{\varepsilon}$ may be decomposed into elastic $\boldsymbol{\varepsilon}^{\mathbf{e}}$ and inelastic $\boldsymbol{\varepsilon}^{\star}$ contributions, *i.e.*

$$\boldsymbol{\varepsilon} = \boldsymbol{\varepsilon}^{\mathbf{e}} + \boldsymbol{\varepsilon}^{\star}. \tag{7}$$

The inelastic deformation components $\boldsymbol{\varepsilon}^{\star}$ may be used to model such things as initial deformations, thermal deformations, eigenstrains, misfit strains, and plastic strains. If any of the aforementioned aspects are modelled in a nonlinear fashion, then it is meant to imply that the inelastic deformations depend on the state of the configuration. Such inelastic deformation components $\boldsymbol{\varepsilon}^{\star}$ may, consequently, modify the effective stiffness of the configuration. Typically, if plastic material behaviour is modelled, the inelastic deformation components are taken to be a function of the stress state itself

$$\boldsymbol{\sigma} = \mathbf{S}(\boldsymbol{\varepsilon} - \boldsymbol{\varepsilon}^{\star}[\boldsymbol{\sigma}, \boldsymbol{\varepsilon}_{\mathbf{q}}]), \quad \boldsymbol{\sigma}_e = \mathbf{S}_e(\boldsymbol{\varepsilon}_e - \boldsymbol{\varepsilon}_e^{\star}[\boldsymbol{\sigma}_e, \boldsymbol{\varepsilon}_{\mathbf{q}_e}]), \tag{8}$$

along with equivalent plastic deformations (internal variables) $\boldsymbol{\varepsilon}_{\mathbf{q}}$. Plastic deformation is modelled to occur if the stress state exceeds the yield surface. The stress term $\boldsymbol{\sigma}_e$ (or $\boldsymbol{\sigma}$) on the right-hand side of Eq. (8), and the representation of the onset of plastic deformation (stress limit), which may depend on the history of the state of the configuration, make the material law (and the static equilibrium conditions which follow) nonlinear. The interested reader is referred to Dhondt [42], for example, for further details.

Regardless of the intricate details of the material law (8), by substitution of the linear (geometric) deformation relations (5) in the virtual work equation (2), one finds that

$$(\mathbf{D}^T\boldsymbol{\sigma})\cdot\delta\mathbf{u} = \mathbf{f}\cdot\delta\mathbf{u}, \tag{9}$$

which should hold true for all kinematically admissible variations $\delta\mathbf{u}$ at static equilibrium. Assuming that prescribed kinematic boundary conditions are dealt with in an appropriate way, the static equilibrium equations for the entire FE model follow as

$$\mathbf{D}^T\boldsymbol{\sigma} = \mathbf{f}. \tag{10}$$

Considering linear structural behaviour: the linear material law (6), the linear deformation relations (5), and the static equilibrium equations (10), culminate in the well-known representation of static equilibrium

$$\mathbf{K}\mathbf{u} = \mathbf{f} + \mathbf{f}^{\star}, \tag{11}$$

in terms of the system-level stiffness matrix $\mathbf{K} = \mathbf{D}^T[\mathbf{0}]\,\mathbf{S}\,\mathbf{D}[\mathbf{0}]$, and the equivalent nodal loads $\mathbf{f}^{\star} = \mathbf{D}^T[\mathbf{0}]\,\mathbf{S}\,\boldsymbol{\varepsilon}^{\star}$ 'induced' by the inelastic deformations (*e.g.* in the modelling of thermomechanics).

Typically, in the presence of nonlinearity, Newton's method,[1] which operates on a variable (preferably consistent) tangent stiffness matrix $\frac{\partial}{\partial\mathbf{u}}(\mathbf{D}^T\boldsymbol{\sigma})[\mathbf{u}]$, evaluated at the current state of the configuration (and the associated equivalent nodal loads), is employed to establish the static equilibrium state. In terms of the computational burden, solving the linear equilibrium conditions (11) is equivalent to a single iteration in Newton's method.

2.2. A single AM process step

In AM process simulation a single process (time) step corresponds to (i) the stress-free merger of a new part of the structural configuration to the existing structural configuration, and (ii) solidification and cooling of the newly added material, causing an increment in the equilibrium state of the configuration. Thus, we have to distinguish between two collections of mechanical field quantities in the configuration. The first collection is the dofs $\underline{\mathbf{u}}$, deformations $\underline{\boldsymbol{\varepsilon}}$, and stresses $\underline{\boldsymbol{\sigma}}$ which measure the state of the structural configuration *prior* to the AM process step. The second collection contains the *additional* dofs $\bar{\mathbf{u}}$, deformations $\bar{\boldsymbol{\varepsilon}}$, and stress $\bar{\boldsymbol{\sigma}}$ components, those associated with the newly added material. An increment relative to the equilibrium state which holds prior to the AM process step, to establish the equilibrium state after the AM process step, is denoted by quantities with a preceding Δ symbol. Fig. 1 is a graphical illustration of what we describe here. In Fig. 1 the grey region represents the existing configuration, the white region indicate the new part of the configuration, and the Δ…'s denote an incremental step in the associated quantity to establish the new static equilibrium state (the state after the process step). Without a loss in generality, external nodal loads are neglected in the presentation of the AM process model.

The complete set of dofs in the extended configuration, prior to the introduction of the increment to establish the new state equilibrium state, is written as

$$\bar{\underline{\mathbf{u}}} = \begin{pmatrix} \bar{\mathbf{u}} \\ \underline{\mathbf{u}} \end{pmatrix}. \tag{12}$$

The same notation is used to denote the complete sets of deformations, stresses, and inelastic deformations, for example

$$\bar{\underline{\boldsymbol{\varepsilon}}} = \begin{pmatrix} \bar{\boldsymbol{\varepsilon}} \\ \underline{\boldsymbol{\varepsilon}} \end{pmatrix} \quad \text{and} \quad \bar{\underline{\boldsymbol{\sigma}}} = \begin{pmatrix} \bar{\boldsymbol{\sigma}} \\ \underline{\boldsymbol{\sigma}} \end{pmatrix}. \tag{13}$$

Importantly, deformation components in the new part of the configuration $\bar{\boldsymbol{\varepsilon}}$ are dependent on some dofs in the pre-existing configuration $\underline{\mathbf{u}}$ (nodes on the old-new configuration interface). This has implications for the representation of the AM process step as 'stress—or strain—free' (common practice in AM process modelling); we return to this aspect further below. Naturally, before the new part of the configuration is introduced, the deformations in the already existing configuration obey (under geometric linearity assumptions)

$$\underline{\boldsymbol{\varepsilon}}[\underline{\mathbf{u}}] = \underline{\mathbf{D}}\underline{\mathbf{u}}, \tag{14}$$

and the stresses follow from the material law, as before

$$\underline{\boldsymbol{\sigma}} = \underline{\mathbf{S}}(\underline{\boldsymbol{\varepsilon}}[\underline{\mathbf{u}}] - \underline{\boldsymbol{\varepsilon}}^0), \tag{15}$$

wherein initial (inelastic) deformations $\underline{\boldsymbol{\varepsilon}}^0$ are introduced to represent the current state of the configuration, representing such quantities as thermal, plastic, or 'inherent' deformations which are present in the existing configuration. Note that, the source (or cause) of the initial (inelastic) deformations $\underline{\boldsymbol{\varepsilon}}^0$ is inconsequential: it is the collection of those (inelastic) deformations which, if subtracted from the total deformation $\underline{\boldsymbol{\varepsilon}}[\underline{\mathbf{u}}]$, yield the *elastic* deformation components on which the material model (15) operates. Having neglected external nodal loads, static equilibrium implies that

$$\underline{\mathbf{D}}^T\underline{\boldsymbol{\sigma}} = \mathbf{0}, \tag{16}$$

wherein handling of the appropriate boundary conditions (*e.g.* baseplate) is implied.

A structural configuration in an AM process exhibits evolving deformation and stress fields due to the transient thermal gradients, (solid-state) phase transformation and nonlinear material behaviour induced by the localized heating, melting, fusion, solidification and cooling of the new and existing parts of the configuration. This culminates in macroscale stress and distortion. However, in order to describe (and model) the merger of a new part of the configuration to the existing configuration, it is useful to first imagine an *ideal* AM process step. That is an AM process step which causes zero thermal gradients, for example, and thereby zero distortion (a zero increment $\Delta\ldots = \mathbf{0}$ in the mechanical field quantities already present prior to the ideal step). An *ideal* AM process step is characterised by a zero change in the inelastic deformation components $\boldsymbol{\varepsilon}^{\star}$, and the new dofs are at zero $\bar{\mathbf{u}} = \mathbf{0}$, reflecting zero distortion. Yet, assuming that, in general, a nonzero displacement field may be present prior to the AM process step, the deformations of the newly added material

$$\bar{\boldsymbol{\varepsilon}}[\bar{\underline{\mathbf{u}}}] = \bar{\mathbf{D}}\begin{pmatrix} \bar{\mathbf{u}} = \mathbf{0} \\ \underline{\mathbf{u}} \neq \mathbf{0} \end{pmatrix}, \tag{17}$$

[1] Also referred to as the Newton-Raphson method.

(a) Equilibrium prior to AM process step (before material addition, solidification and cooling)

(b) Equilibrium after AM process step (after material addition, solidification and cooling)

Fig. 1. Sets of mechanical field quantities considering an AM process step.

may be nonzero, due to the dependency on the dofs in the pre-existing configuration $\underline{\mathbf{u}}$. This is associated with nonzero stress components and a static equilibrium imbalance, generating an increment in the static equilibrium state $\Delta\ldots$. That is *distortion*—-not an ideal AM process step. In order to describe an *ideal* AM process step, initial deformation components equated to the deformation mismatch between the existing and new part of the configuration

$$\bar{\varepsilon}^0[\bar{\mathbf{u}}] = \bar{\mathbf{D}}\begin{pmatrix}\bar{\mathbf{u}} = \mathbf{0}\\ \underline{\mathbf{u}}\end{pmatrix}, \tag{18}$$

are included in the material law, which, in turn, causes the stress components to vanish

$$\bar{\sigma} = \bar{\mathbf{S}}(\bar{\varepsilon}[\bar{\mathbf{u}}] - \bar{\varepsilon}^0[\bar{\mathbf{u}}]) = \mathbf{0}. \tag{19}$$

Physically speaking, the liquid state of the (melted) material when the new part of the configuration is seen to merge (perfectly) with the existing part, is taken to imply that the new part is connected *stress-free*. Therefore, static equilibrium of the new, extended configuration—with the ideally merged, new part of the structure, connected—dictates that

$$\bar{\mathbf{D}}^T\bar{\sigma} = \mathbf{0}, \tag{20}$$

wherein the extended deformation-dof differentiation matrix $\bar{\mathbf{D}}$ is taken to define the (linear) relation

$$\bar{\varepsilon}[\bar{\mathbf{u}}] = \bar{\mathbf{D}}\bar{\mathbf{u}}, \tag{21}$$

as before, but with respect to the extended configuration.

The static equilibrium conditions (20), after an *ideal* AM process step, imply a zero change in the pre-existing dofs $\underline{\mathbf{u}}$ and the new dofs $\bar{\mathbf{u}}$, deformations $\bar{\varepsilon}$ and stresses $\bar{\sigma}$. That is to say, the new dof components $\bar{\mathbf{u}}$ retain their reference values $\bar{\mathbf{u}} = \mathbf{0}$ at the existing static equilibrium state, and static equilibrium of the pre-existing structure is not affected. Having no misfit between the existing and new part of the structural configuration at the moment an element (or layer) is activated, is referred to as a 'strain-free model change' in some contemporary FE analysis packages [43]. This is also closely related to element 'birth-and-death' techniques in welding simulation—see for example Chen et al. [44].

The distortions and residual stresses associated with an actual (not ideal) AM process step is caused by an increment in the inelastic deformation components

$$\bar{\varepsilon}^0 + \Delta\bar{\varepsilon}^\star = \begin{pmatrix}\bar{\varepsilon}^0 + \Delta\bar{\varepsilon}^\star\\ \underline{\varepsilon}^0 + \Delta\underline{\varepsilon}^\star\end{pmatrix}, \tag{22}$$

and a corresponding increment in the static equilibrium state

$$\bar{\mathbf{D}}^T(\bar{\sigma} + \Delta\bar{\sigma}) = \mathbf{0}, \tag{23}$$

according to the material law

$$\bar{\sigma} + \Delta\bar{\sigma} = \bar{\mathbf{S}}(\bar{\varepsilon}[\bar{\mathbf{u}}] + \Delta\bar{\varepsilon}[\Delta\bar{\mathbf{u}}] - \bar{\varepsilon}^0 - \Delta\bar{\varepsilon}^\star). \tag{24}$$

To be clear: the $\ldots^0$ terms denote initial deformations, either present in the existing configuration, and/or required to merge material stress free; while the $\ldots^\star$ terms denote inelastic deformation increments, seen to model the inelastic deformations induced by the process. Typically, in SLM process modelling, the predetermined inherent (inelastic) deformation components are applied to the new material layer in each step of the process. In general however, the inelastic deformation increment associated with the process step may extend into the old part of the configuration.

In the geometrically linear AM process model, it is the nature of the inelastic deformation component increments $\Delta\underline{\varepsilon}^\star$ which determine whether the process step is linear or nonlinear. For example, if an one-way coupled linear thermomechanical analysis is conducted, then the increments $\Delta\underline{\varepsilon}^\star$ are a function of the temperature field and the material expansion coefficients. However, computation of the mechanical response $\Delta\underline{\mathbf{u}}$ requires a single linear analysis. If nonlinear plastic deformations form part of the inelastic deformation component increment $\Delta\underline{\varepsilon}^\star$, then the process step is nonlinear.

2.3. Linearisation of the AM process model

It is clear to see that linearity assumptions permit the expression of the static equilibrium equations (23), subsequent to the AM process step, in superimposed form

$$\bar{\mathbf{D}}^T\bar{\sigma} + \bar{\mathbf{D}}^T\Delta\bar{\sigma} = \mathbf{0}. \tag{25}$$

The components relating to the existing equilibrium state (16), expanded to the extended configuration with the notion of an ideal (stress-free) AM process step (20), are known to be in balance. Therefore, the incremental component

$$\bar{\mathbf{D}}^T\Delta\bar{\sigma} = \mathbf{0}, \tag{26}$$

may be computed independent of the current state of the configuration $\bar{\mathbf{u}}$, in terms of an incremental material law

$$\Delta\bar{\sigma} = \bar{\mathbf{S}}(\Delta\bar{\varepsilon} - \Delta\bar{\varepsilon}^\star). \tag{27}$$

As before, the static equilibrium increment may be written in terms of the (newly extended) system-level stiffness matrix

$$\bar{\mathbf{K}}\Delta\bar{\mathbf{u}} = \Delta\bar{\mathbf{f}}^\star, \tag{28}$$

and the increment in the equivalent nodal loads; that is $\bar{\mathbf{K}} = \bar{\mathbf{D}}^T[\mathbf{0}]\,\bar{\mathbf{S}}\,\bar{\mathbf{D}}[\mathbf{0}]$, and $\Delta\bar{\mathbf{f}}^\star = \bar{\mathbf{D}}^T[\mathbf{0}]\,\bar{\mathbf{S}}\,\Delta\bar{\varepsilon}^\star$, respectively. Notice how the initial deformations $\bar{\varepsilon}^0$, required to fit the new part of the configuration to the old part in a stress-free manner, and, for the representation of the current state of the configuration, have dropped out: a static increment is computed with respect to a stress-free reference configuration. Inelastic deformation increments in either or both the pre-existing or new part of the configuration $\Delta\bar{\varepsilon}^\star$ are taken to be representative of thermal deformations, or predetermined inherent deformations, for example. The linear formulation of the AM process model permits quick and easy computation of the equilibrium state of the configuration. The incremental conditions for static equilibrium after each process step (26) and the quantities required in the definition of the material law (27), render the relative increment in the state of the configuration (28) computable completely independent of what went before. The implication is that the static equilibrium increment generated by each and every process step in the linear AM simulation may be computed *independently and in parallel*.

Now, consider a total of P linear AM process steps, each of which turns out to be a static equilibrium increment with respect to the

corresponding (stress-free) reference configuration

$$\bar{\underline{\mathbf{K}}}^{\{p\}}\Delta\bar{\underline{\mathbf{u}}}^{\{p\}} = \Delta\bar{\underline{\mathbf{f}}}^{\{p\}\star}, \tag{29}$$

for $p = 1, 2, \ldots, P$. If we permit ourselves to conduct summation operations on arrays of different sizes—for notational convenience—the final dofs, relative to the reference configuration $\bar{\underline{\mathbf{u}}}^0$, are easily rendered according to

$$\bar{\underline{\mathbf{u}}}^{\{P\}} = \sum_{p=1}^{P} \Delta\bar{\underline{\mathbf{u}}}^{\{p\}}. \tag{30}$$

That is to say, the dof (displacement) components which are not yet present in the particular configuration after process step p, are taken to be zeros (the computationally minded reader may be reminded of sparse storage formats and matrix-vector operations). In the final equilibrium state of the configuration, the accumulated inelastic deformation components

$$\sum_{p=1}^{P} \Delta\bar{\underline{\boldsymbol{\varepsilon}}}^{\{p\}0} + \sum_{p=1}^{P} \Delta\bar{\underline{\boldsymbol{\varepsilon}}}^{\{p\}\star} \tag{31}$$

adhere to the material law

$$\bar{\underline{\boldsymbol{\sigma}}}^{\{P\}} = \bar{\underline{\mathbf{S}}}^{\{P\}}\left(\bar{\underline{\boldsymbol{\varepsilon}}}^{\{P\}}[\bar{\underline{\mathbf{u}}}^{\{P\}}] - \sum_{p=1}^{P} \Delta\bar{\underline{\boldsymbol{\varepsilon}}}^{\{p\}0} - \sum_{p=1}^{P} \Delta\bar{\underline{\boldsymbol{\varepsilon}}}^{\{p\}\star}\right), \tag{32}$$

with the stress components governed, in turn, by the conditions of static equilibrium

$$\bar{\underline{\mathbf{D}}}^{\{P\},T}\bar{\underline{\boldsymbol{\sigma}}}^{\{P\}} = \mathbf{0}. \tag{33}$$

The $\Delta\bar{\underline{\boldsymbol{\varepsilon}}}^{\{p\}0}$ terms are intended to show that, in general, any number of process steps may contribute to the misfit deformation which is present when a new part of the configuration is connected $\bar{\underline{\boldsymbol{\varepsilon}}}^{\{p\}0}$, but the computation of the final equilibrium state is an independent summation of the process step increments, nevertheless. It is expected (imagining the physics of the process) that a linear material law may not yield an accurate representation of the stress state of the configuration. However, the displacement dofs may be accurate, particularly if the inelastic deformation components are calibrated to experimental distortion data. To incorporate a nonlinear material law in the linear AM process simulation outlined above, we consider the following computationally-minded approximation: having combined (superimposed) all the increments to construct the final equilibrium state (33), the linear elastic material law (32) is replaced by an elastoplastic material law, as defined in (8), and the increment to establish the new equilibrium state is computed. This type of nonlinear static equilibrium computation is of course required in every process step (and trivial process-step parallel computability breaks down) if nonlinear plastic material behaviour is modelled throughout the process, often leading to a prohibitive computational burden. Geometrically nonlinear structural behaviour, on the other hand, is expected to be mild (if present at all) in the structural geometries considered herein (which are neither thin-walled nor slender).

3. Numerical implementation, demonstrations, and experiments

3.1. Implementation and deposition order

In Fig. 2 flowcharts of the conventional (sequential) AM process simulation (left) and the parallel process-step AM simulation (right) is given. Throughout, to *compute static equilibrium* is meant to imply that a set of equations of the form

$$\bar{\underline{\mathbf{K}}}^{\{p\}}(\bar{\underline{\mathbf{u}}}^{\{p\}} + \Delta\bar{\underline{\mathbf{u}}}^{\{p\}}) = \bar{\underline{\mathbf{f}}}^{\{p\}\star} + \Delta\bar{\underline{\mathbf{f}}}^{\{p\}\star}, \quad \text{or} \quad \bar{\underline{\mathbf{K}}}^{\{p\}}\Delta\bar{\underline{\mathbf{u}}}^{\{p\}} = \Delta\bar{\underline{\mathbf{f}}}^{\{p\}\star}, \tag{34}$$

is assembled and solved. In the sequential setting (left), the equilibrium state is updated according to $\bar{\underline{\mathbf{u}}}^{\{p+1\}} \longleftarrow \bar{\underline{\mathbf{u}}}^{\{p\}} + \Delta\bar{\underline{\mathbf{u}}}^{\{p\}}$, *etc.*, for each process step $p = 1, 2, \ldots, P$. In the independent (parallel computable) process-step setting, the final equilibrium state is computed at once

$$\bar{\underline{\mathbf{u}}}^{\{P\}} \longleftarrow \sum_{p=1}^{P} \Delta\bar{\underline{\mathbf{u}}}^{\{p\}}. \tag{35}$$

In order to demonstrate some properties of the AM process simulation framework detailed above, a 100 × 100 × 100 mm cube geometry, discretized with 1000 equally-sized eight-noded brick elements, is employed. See Flanagan and Belytschko [45] for details of the element. All the displacement components on the lower surface of the cube are fixed at zero (representative of baseplate-boundary-conditions). The material is taken to be isotropic, with a constant Young's modulus of 125 GPa and a Poisson ratio of 0.333. Each process step is taken to cause an isotropic increment in the inelastic deformation components associated with the new part of the configuration (the new layer or block in that step), with the relevant components prescribed at $\Delta\bar{\varepsilon}_j^{\{p\}\star}$ = -0.005. This value is taken to be representative of a thermal contraction from the melting temperature of the material to the temperature of the build chamber—see Appendix A. Two AM process discretizations are considered, as depicted in Fig. 3. The first (left) is a depiction of a layer-by-layer AM process discretization; the second (right) shows a block-wise AM process discretization, with an alternative deposition order. The former is standard practice in SLM process models, while the latter is more reminiscent of directed material deposition—*e.g.* wire-feed or blown powder—processes. Note that we here assume that the effects of respective scanning patterns and other detailed process characteristics can be captured in a tailored inherent strain tensor.

The linear AM simulation conducted as per the layer-by-layer discretization yields the distortion prediction depicted in Fig. 4. The distortion predictions yielded by the block-wise AM simulation is given in Fig. 5.[2] In the linear AM process simulation reported above, it is irrelevant whether the depicted equilibrium states were computed with a sequential or parallel process-step implementation—the results are exactly the same in the linear regime. This numerical experiment confirms and validates our theory that the superposition principle still applies to linearized AM process simulations on growing structural domains. The examples given of two different AM process discretizations are intended to emphasise that independent parallel computability of the process-step increments hold all the same. The block-wise-case is intended to show that the process need not be *layer-wise*, and that any number of process steps may contribute to the misfit deformation which is present at the moment a new part of the configuration is activated. In general, after each independent static equilibrium increment computation, the deformations present in the part of the reference configuration which is not yet deposited (or solidified) are recorded—this does not, however, involve a static equilibrium computation. Subsequently, the accumulated initial deformation increments are superimposed to render the equilibrium state after some process step of interest (after the build, for example). In the layer-by-layer case the aforementioned procedure is simpler because only one process step contributes to the initial deformation which is present when a layer is merged to the configuration—in a sequential simulation, it is the displacement and deformation caused by the merger of the layer that went immediately before.

3.2. Distortion and stress predictions

In the linear elastic simulation, yielding of the material is not modelled to occur. Therefore, it is expected that the stress field will be

[2] Note that it is the (amplified) warpage of the geometry which makes it seem that the displacement field is discontinuous in (d), as a number of elements become hidden in the visualisation. This is not the case, see (c) by comparison. The equilibrium state *always* satisfies the same continuity, material and equilibrium laws as in the equivalent sequential simulation.

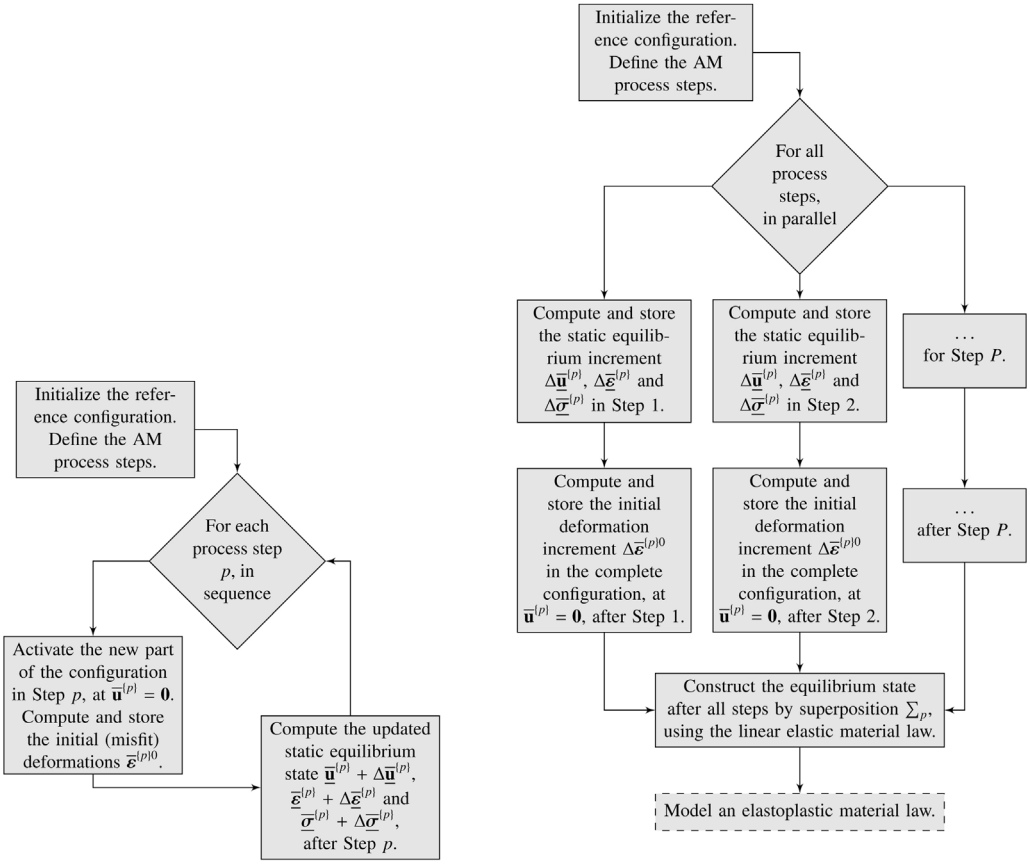

(a) Sequential process steps (b) Parallel process steps with a posterior elastoplastic step

Fig. 2. Flowchart representations of sequential AM process simulation (a) and parallel process-steps with an appended elastoplastic material law (b).

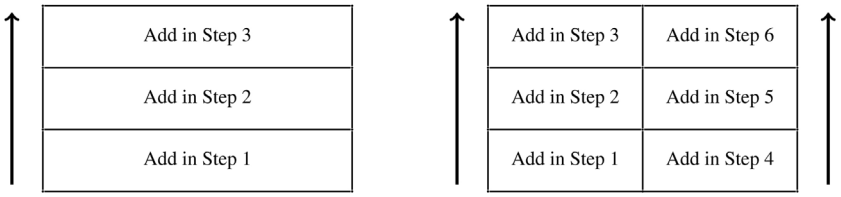

(a) Layer-wise AM process discretization (b) Block-wise AM process discretization

Fig. 3. Illustration of layer-wise and block-wise AM process discretizations.

overestimated. The final equilibrium state is the starting point for the modelling of the 'posterior' elastoplastic material law, to the end of (more) accurate stress predictions. To show the effect of this, the conventional, sequential, nonlinear elastoplastic AM simulation is compared to the linear elastic simulation (with independent process-step increments), followed by the imposition of an elastoplastic material law. Because material nonlinearity is present in every process step in the *former*, linear superposition and parallel process-step computation is not available—and the simulation may be time-consuming. Here we consider only the layer-by-layer version of the process, applied to the

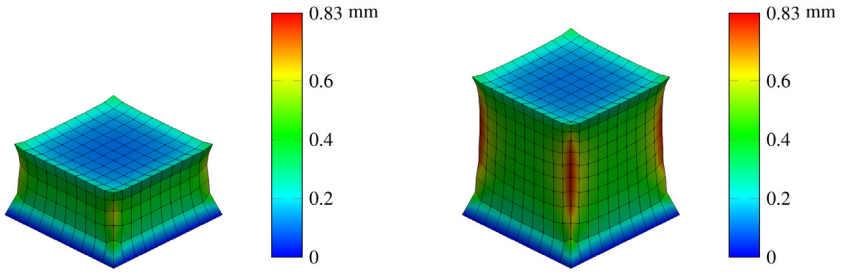

(a) Step 5; magnitude of distortion. (b) Step 10; magnitude of distortion.

Fig. 4. Layer-wise AM process simulation of a 10-step process, 100 × 100 × 100 mm cube build, discretized with 10 × 10 × 10 FE's. Plots of the magnitude of the distortion vector after Step 5 and Step 10. Geometry warpage amplified by a factor of 20.

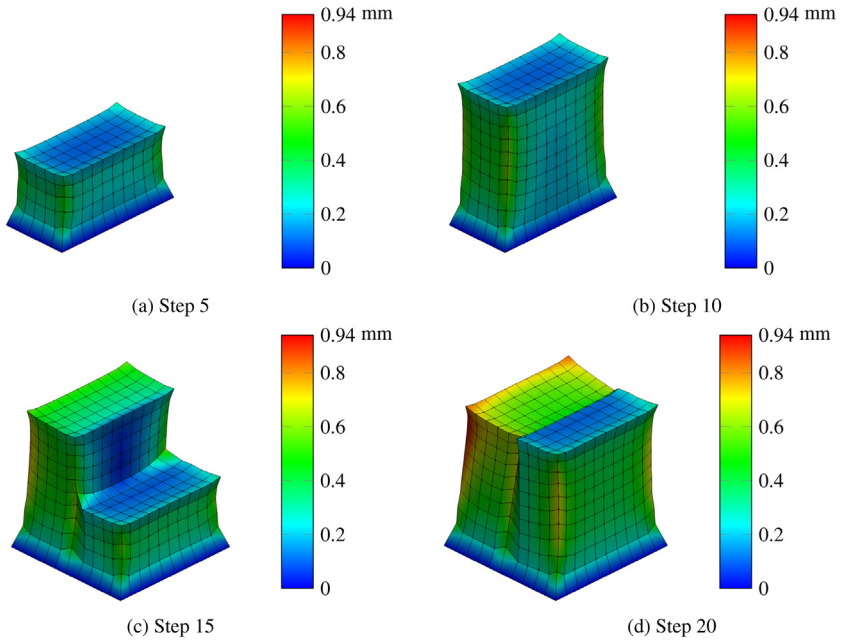

Fig. 5. Block-wise AM process simulation of a 20-step process, 100 × 100 × 100 mm cube build, discretized with 10 × 10 × 10 FE's. Plots of the magnitude of the distortion vector after Step 5, 10,15 and 20. Geometry warpage amplified by a factor of 20.

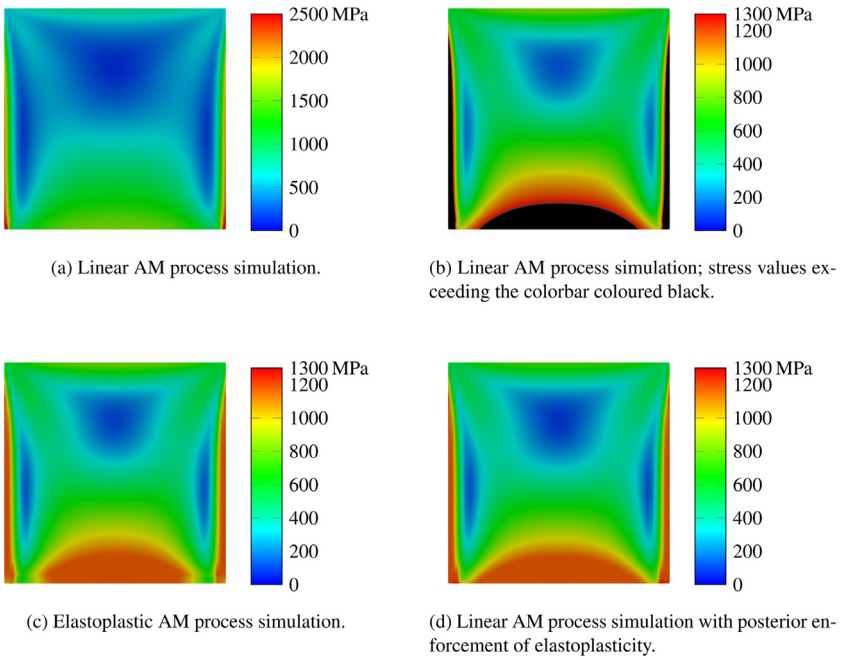

Fig. 6. Predicted von Mises stress fields at mid section of the 100 × 100 × 100 mm cube, layer-wise build: (a) and (b) linear AM process simulation; (c) elastoplastic AM process simulation; (d) linear AM proves simulation with posterior enforcement of an elastoplastic material law.

100 × 100 × 100 mm cube from above, but discretized with 50 elements along each coordinate axis. In all cases, the yield curve is taken from Mukherjee et al. [33]. In Fig. 6a the von Mises stress field predicted by the linear elastic AM process simulation is plotted. In order to study the predicted stress fields, a section midway through the cube is considered. In Fig. 6c the von Mises stress field predicted by the sequential, elastoplastic AM process simulation, is depicted. For the sake of comparison, the stress field corresponding to the linear elastic AM process simulation is plotted again in Fig. 6b, but limited at the maximum value of the elastoplastic simulation. In Fig. 6d the von Mises stress field computed with the imposition of the nonlinear elastoplastic material, after the final equilibrium state of the linear elastic simulation is obtained, is plotted. Clear to see is that the imposition of a posterior elastoplastic material law leads to reduction of the stress field to reasonable values. In Fig. 7 the corresponding distortion predictions are plotted (on warped geometries). At close inspection it is possible to discern that the elastoplastic simulation and the posterior elastoplastic simulation correspond well along the verticals of the corners of the cube, whereas a slight discrepancy occurs at the uppermost layer due to (re)equilibriation of the stresses.

To gain some insight into the possibility of encroaching into the geometrically nonlinear regime, numerical experiments with geometrically nonlinear behaviour included in the linear elastic simulation, with increasing multiples of the inelastic deformation increment, are

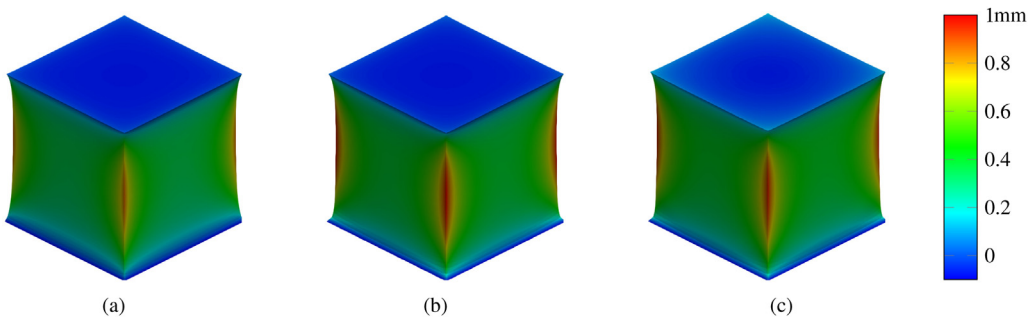

Fig. 7. Plots of distortion (magnitude) of the 100 × 100 × 100 mm cube, layer-wise build: (a) linear elastic (b) elastoplastic, and (c) posterior plastic; geometries warped ×10.

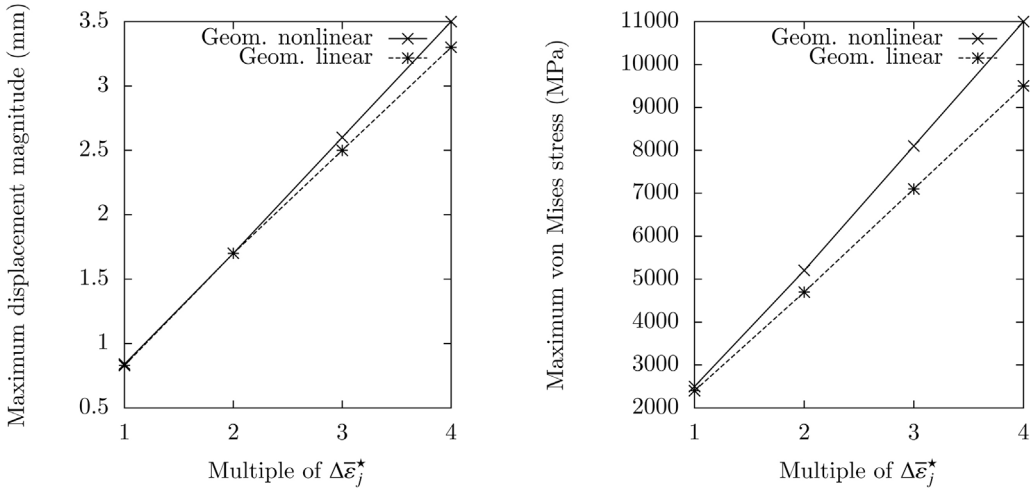

(a) Maximum displacement magnitude (b) Maximum von Mises stress

Fig. 8. Comparison of distortion and stress quantities predicted by a linear and geometrically nonlinear AM process simulations, for increasing inelastic deformation increments.

conducted. In Fig. 8 the maximum displacement magnitude and von Mises stress is plotted, for multiples of the inelastic deformation increment introduced above. It is clear to see, for the simple structural geometry considered here—which is neither thin-walled nor slender—geometrically nonlinear behaviour is hardly observed, even for excessive inelastic deformation increments. That is to say, layer-by-layer element activation ('strain-free' model changes) and inelastic deformation increments do not introduce any additional or unconventional geometric nonlinearities.

The simple (cube) structural geometry studied here is of course by no means indicative of the behavior and predictions of the simulation procedures, in general. With this simple geometry we wish merely to highlight some basic mechanical aspects, and future work is planned for comparison with and calibration to physical experiments.

3.3. Simulation wall-clock time

Next, the speed-up in wall-clock time which may be achieved by exploiting parallel process-step computability in the linear regime, is reported. For the sake of brevity, we consider only the layer-wise version of the AM process model. It is obvious that the necessity of Newton's method (typically) in every step of the sequential, nonlinear elastoplastic simulation, is much more time-consuming than the linear case appended with an elastoplastic step. The wall-clock times required to simulate each process step in the layer-wise AM build independently and in parallel, followed by superposition, are measured, and summarised in Table 1. The structural configurations range from small—10 layers made-up of 1000 elements (10 × 10 × 10) in total—to large—refined to 100 layers, made-up of 1 000 000 elements (100 × 100 × 100) in total. Please note, mesh-refinement is done with respect to all the axes, not only the printing direction. The wall-clock times required using a 4-core laptop architecture (i7-4770HQ CPU @ 2.20 GHz, 7.7 GB RAM), considering the 10–50 layer AM builds, are plotted in Fig. 9a. Using more than one core, the parallel process-steps are arranged in such a way that each core is tasked with roughly an equal computational burden (in terms of the sizes of the configurations corresponding to each process-step increment). Using 2 cores, wall-clock time is halved. Using 3 and 4 cores, wall-clock time is reduced proportionally, although the relative speed-up diminishes slightly with respect to the ideal due to summation operation carried out at the end

Table 1
Problem sizes for wall-clock time measurements of parallel process-step computation and superposition.

Layers	Per layer		Total	
	Elements	dofs	Elements	dofs
10	100	363	1000	3993
20	400	1323	8000	27 783
30	900	2883	27 000	89 373
40	1600	5043	64 000	206 763
50	2500	7803	125 000	397 953
60	3600	11 163	216 000	680 943
70	4900	15 123	343 000	1 073 733
80	6400	19 683	512 000	1 594 323
90	8100	24 843	729 000	2 260 713
100	10 000	30 603	1 000 000	3 090 903

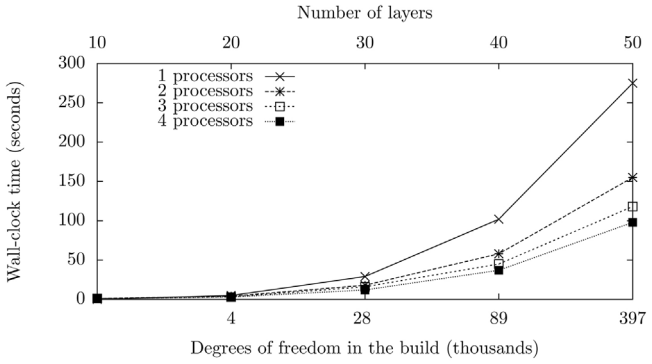

(a) Small-scale parallel process-step computation (laptop)

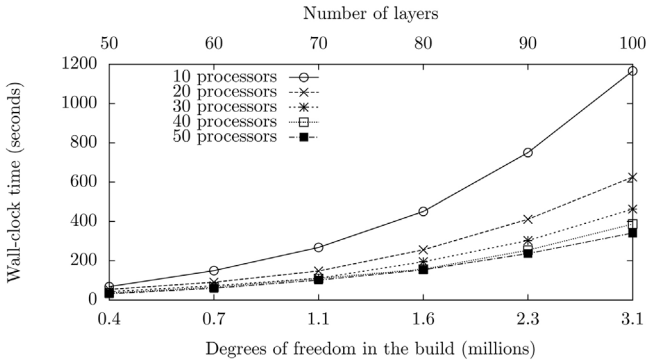

(b) Large-scale parallel process-step computation (cluster)

Fig. 9. Wall-clock time required for layer-wise AM process simulation exploiting parallel process-step computation.

(which is not parallelized here). The wall-clock times achieved on a computational cluster, applying 10–50 cores on the 50–100 layer builds, are reported in Fig. 9b.

The same wall-clock time scaling as in the small-scale (laptop) setting is observed. This is quite remarkable, as conventional domain-level parallelization techniques rarely achieve wall-clock time scaling in this way, approaching the ideal. For both the small—and large-scale implementations a modified version of CalculiX [46] (a free and open-source FE analysis code) is used. We can report that the default domain-level parallelization procedures implemented in CaluculiX (*i.e.* applied in a conventional sequential simulation) yield nowhere the same amount of speedup: 4 cores require over 1000 s to simulate the 40 layer case. In Section 3.4 wall-clock times are compared to domain-level parallelization in the equivalent Abaqus simulation, considering an industrial build. The wall-clock time measurements reported here show that process-step parallelization is faster than domain-level parallelization techniques, and reasonable wall-clock time scaling can be achieved with this simple avenue of AM process simulation. Moreover, process-step parallel computation illustrates rather nicely the nature of AM process simulation in the linear regime.

3.4. Industrial test case

Here we present and discuss the application of the method to a distortion prediction of a layer-wise AM simulation (representative of an SLM process), conducted on an industrial structural geometry. In Fig. 10a and b two views of an STL representation of the considered part, are given. The part is voxelised based on a regular grid suited to a layer-by-layer process, assuming the interior is 100% filled. (Homogenization techniques may be resorted to capture fine structural features on relatively coarse meshes.) The regular grid forms a natural starting point for a hexagonal FE discretization. The part is enclosed by $128 \times 119 \times 100$ elements, with a characteristic length of 1 mm. That is, the simulation comprises 100 process steps. The corresponding views of the voxelised part are given in Fig. 10c and d. As before, each process step involves an inelastic deformation increment applied to the uppermost layer of the structural configuration deemed to be in existence at that point in the process. The material properties are retained from before. The simulation quantities are representative of a generic Ti-6AL-4V SLM process.

For the sake of comparison, two AM simulation methodologies are considered: conventional, sequential simulation with elastoplastic material behavior and geometric nonlinearity taken into account *vs.* the step-wise parallel linear elastic simulation, as delineated in this paper.

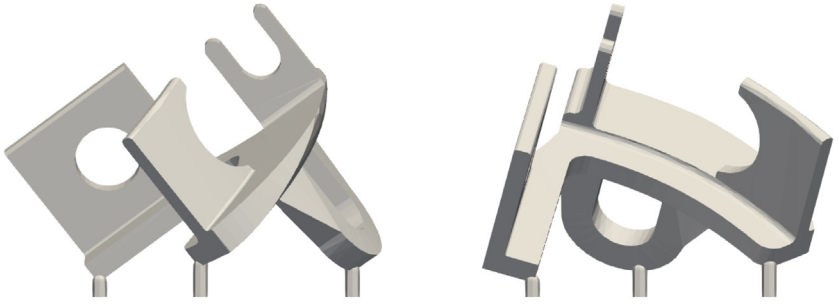

(a) STL model (View 1) (b) STL model (View 2)

(c) Voxelised model (View 1) (d) Voxelised model (View 2)

Fig. 10. Industrial test case $128 \times 119 \times 100$ mm: STL model (a,b), voxelised model (c,d).

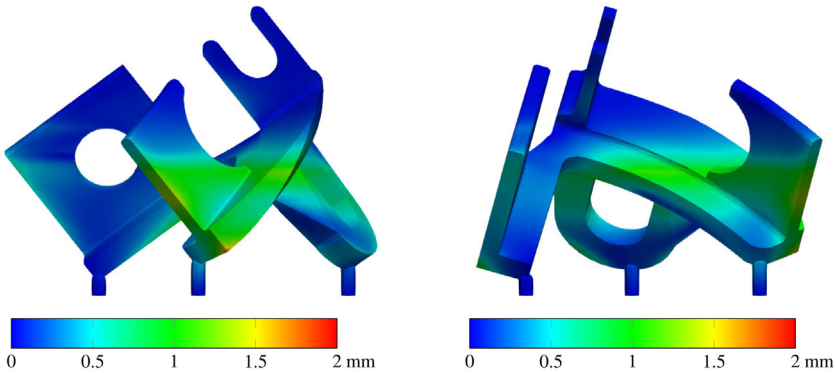

(a) Sequential nonlinear simulation (View 1)

(b) Sequential nonlinear simulation (View 2)

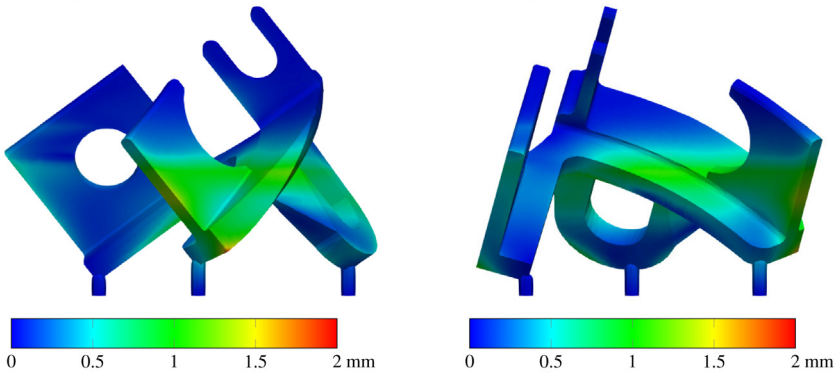

(c) Step-wise parallel simulation (View 1)

(d) Step-wise parallel simulation (View 2)

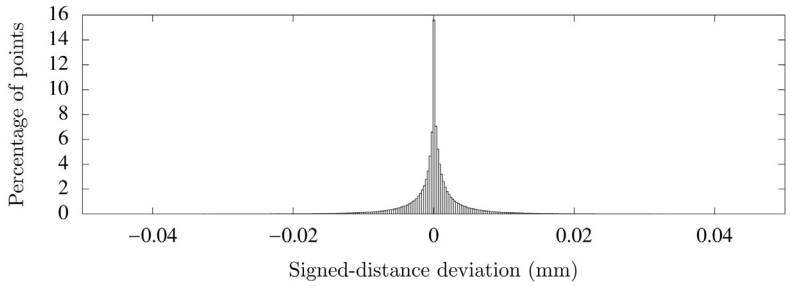

(e) Histogram of deviation analysis.

Fig. 11. Industrial test-case distortion predictions; sequential simulation with elastoplasticity and geometric nonlinearity taken into account (a,b), linear, step-wise parallel simulation (c,d).

In Fig. 11a and b two views of the distortion predicted by the sequential nonlinear simulation are given. In Fig. 11c and d the corresponding views of the distortion prediction yielded by the step-wise parallel linear elastic simulation are given. The displacement field is evaluated on the STL surface via the element interpolation functions, in each case. Based on this depiction of the part distortion, there is little to no difference between the distortion predictions yielded by the sequential nonlinear and the linear, step-wise parallel simulations. In Fig. 11e a histogram plot of a deviation analysis of the two distortion predictions is given. The part geometry is warped with both displacement fields (sequential, nonlinear and step-wise linear). Following this, points are sampled on the part warped with the result of the linear simulation, and a deviation analysis to the reference geometry (warped according to the sequential nonlinear simulation) is conducted. The mean discrepency is 0.00011 mm, and the standard deviation of the discrepancy is 0.00518 mm. That is, about 95% of the warped geometries agree within 10 μm.

Finally, we compare the wall-clock time speed-up achieved with a conventional, commercial FE simulation package, and the method of process-step parallelization—valid under linearity assumptions—delineated herein. The commercial FE simulation package is Abaqus, with default settings, utilizing domain-level parallelization in each sequential step. In both cases the linear elastic simulation conducted above, is repeated. In Fig. 12a the wall-clock times are reported, using 1–6 cores. The results indicate that the Abaqus simulation is associated with a substantial amount more computational overhead, although it should be noted that the simulations could not be conducted on exactly the same hard-ware platforms (although similar). Nevertheless, comparison of the absolute wall-clock time is not the main purpose of this investigation. To discern more clearly the relative speed-up achieved with the different methods of parallelization, the wall-clock times are normalised with the single-core time in each case, and plotted on a log-scale in Fig. 12b. A line representing the theoretically ideal speed-up which may be achieved is included for the sake of comparison. These results show quite clearly that process-step parallelization, available under linearity assumptions, provides a better speed-up—close to ideal—compared to the conventional domain-level parallelization utilized in state-of-the-art commercial FE software.

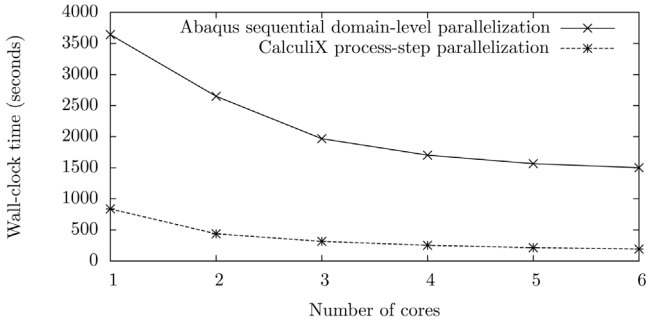

(a) Wall-clock time comparison

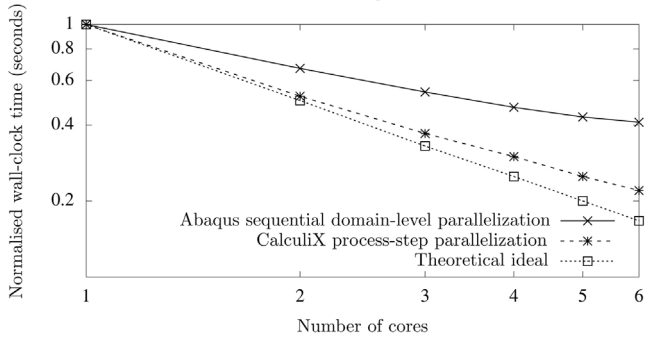

(b) Wall-clock times normalised with single-core times, including theoretical ideal

Fig. 12. Wall-clock time comparison of standard domain-level parallelization and process-step parallelization.

4. Concluding discussion

In closing we wish to state clearly that the total computational burden is not decreased under process-step parallel computation of AM simulation, only wall-clock time. However, parallel computability of the process steps—confined to the linear elastic regime—is a simple avenue of reasonably fast AM simulation, with the potential to mitigate the severe wall-clock-time scaling of the simulation with respect to finer mesh and process discretizations.

The fact that the mechanical aspect of the AM process may be represented and computed in this fashion elucidates the computational structure which underlie AM process models. In particular, the notion that a new part of the configuration is merged to the existing configuration in a stress-free manner; a notion necessitated to describe the trivial case of an ideal AM process step. Moreover, the fact that linearity assumptions imply that a static equilibrium increment in each step of the process is computed with respect to the stress-free reference configuration in existence at that point in time. In the end, the development of fast AM simulation techniques will aid designers in predicting the responses due to AM processes, which enables the study of computational design-for-manufacturing—*e.g.* topology optimization embedded with AM process simulation responses—and process parameter optimization with efficient gradient-based techniques.

Further exploration of combining optimization and AM process simulation forms a clear direction for future research, as well as the experimental validation of the obtained designs.

Acknowledgments

The work forms part of the DISTRACTION project, funded by the European Union's Horizon 2020 research and innovation progamme under Grant Agreement No. 686808. Collaboration with IK4-Lortek Research Alliance and Airbus Structures Research, particularly Iñaki Setien and Sjoerd van der Veen, is gratefully acknowledged.

Appendix A. Isotropic inelastic deformation approximation

We consider the thermal deformation components which arise due to temperature equilibration from the melting temperature of the material T_m to the temperature of the build chamber T_0. Herein a simple isotropic representation of the thermal stress components

$$\Delta\sigma^* = \int_{T_m}^{T_0} E[T]\alpha[T]\mathrm{d}T, \tag{A.1}$$

wherein $E[T]$ and $\alpha[T]$ is the temperature dependent Young's modulus and thermal expansion coefficient of the material, is considered. The accumulated thermal stress is normalised with the material stiffness at the temperature of the build chamber

$$\Delta\varepsilon^* = \frac{\Delta\sigma^*}{E(T_0)}, \tag{A.2}$$

to obtain representative inelastic deformations components. Using the temperature dependent material properties kindly published by Mukherjee et al. [33], a value of -0.006 is obtained—in the numerical experiments we take it as -0.005.

References

[1] I. Gibson, D.W. Rosen, B. Stucker, Additive Manufacturing Technologies vol. 238, Springer, 2010.
[2] A. Nickel, D. Barnett, F. Prinz, Thermal stresses and deposition patterns in layered manufacturing, Mater. Sci. Eng. A 317 (1) (2001) 59–64.
[3] T. Simpson, Easing into AM [Online], (2017) Available from: http://www.mmsonline.com/columns/easing-into-am [17.07.17].
[4] V. Safronov, R. Khmyrov, D. Kotoban, A. Gusarov, Distortions and residual stresses at layer-by-layer additive manufacturing by fusion, J. Manuf. Sci. Eng. 139 (3) (2017) 031017.
[5] W. Gao, Y. Zhang, D. Ramanujan, K. Ramani, Y. Chen, C.B. Williams, C.C. Wang, Y.C. Shin, S. Zhang, P.D. Zavattieri, The status, challenges, and future of additive manufacturing in engineering, Comput.-Aided Des. 69 (2015) 65–89.
[6] Y. Huang, M.C. Leu, J. Mazumder, A. Donmez, Additive manufacturing: current state, future potential, gaps and needs, and recommendations, J. Manuf. Sci. Eng. 137 (1) (2015) 014001.
[7] D. Mourtzis, M. Doukas, D. Bernidaki, Simulation in manufacturing: review and challenges, Proc. CIRP 25 (2014) 213–229.
[8] The Economist, 3D Printers Start to Build Factories of the Future [Online], (2007) Available from: https://www.economist.com/news/briefing/21724368-recent-advances-make-3d-printing-powerful-competitor-conventional-mass-production-3d [29.06.17].
[9] The Economist, 3D Printing Transforms the Economics of Manufacturing [Online], (2017) Available from: https://www.economist.com/news/briefing/21724369-additive-manufacturing-abandons-economies-scale-3d-printing-transforms-economics [01.07.17].
[10] The Economist, 3D Printers Will Change Manufacturing [Online], (2017) Available from: https://www.economist.com/news/leaders/21724397-sceptics-doubt-technology-can-be-used-mass-production-just-wait-3d-printers-will-change [29.06.17].
[11] E. Atzeni, A. Salmi, Economics of additive manufacturing for end-usable metal parts, Int. J. Adv. Manuf. Technol. 62 (9) (2012) 1147–1155.
[12] D. Munro, A Contemplation on Topology Optimization [Online], (2016) Available from: http://www.digitaleng.news/de/a-contemplation-on-topology-optimization/ [31.07.17].
[13] M. Megahed, H.-W. Mindt, N. N'Dri, H. Duan, O. Desmaison, Metal additive-manufacturing process and residual stress modeling, Integr. Mater. Manuf. Innov. 5 (1) (2016) 1–33.
[14] J.-P. Kruth, L. Froyen, J. Van Vaerenbergh, P. Mercelis, M. Rombouts, B. Lauwers, Selective laser melting of iron-based powder, J. Mater. Process. Technol. 149 (1)

(2004) 616–622.
[15] P. Mercelis, J.-P. Kruth, Residual stresses in selective laser sintering and selective laser melting, Rapid Prototyp. J. 12 (5) (2006) 254–265.
[16] J.-P. Kruth, J. Deckers, E. Yasa, R. Wauthlé, Assessing and comparing influencing factors of residual stresses in selective laser melting using a novel analysis method, Proc. Inst. Mech. Eng. Part B: J. Eng. Manuf. 226 (6) (2012) 980–991.
[17] I. Yadroitsev, I. Smurov, Selective laser melting technology: from the single laser melted track stability to 3D parts of complex shape, Phys. Proc. 5 (2010) 551–560.
[18] D. Gu, F. Chang, D. Dai, Selective laser melting additive manufacturing of novel aluminum based composites with multiple reinforcing phases, J. Manuf. Sci. Eng. 137 (2) (2015) 021010.
[19] S. Ghosh, J. Choi, Three-dimensional transient finite element analysis for residual stresses in the laser aided direct metal/material deposition process, J. Laser Appl. 17 (3) (2005) 144–158.
[20] L. Löber, C. Flache, R. Petters, U. Kühn, J. Eckert, Comparison of different post processing technologies for SLM generated 316l steel parts, Rapid Prototyp. J. 19 (3) (2013) 173–179.
[21] U. Tradowsky, J. White, R. Ward, N. Read, W. Reimers, M. Attallah, Selective laser melting of AlSi10Mg: influence of post-processing on the microstructural and tensile properties development, Mater. Des. 105 (2016) 212–222.
[22] N. Klingbeil, J. Beuth, R. Chin, C. Amon, Measurement and modeling of residual stress-induced warping in direct metal deposition processes, Solid Freeform Fabrication Symposium (1998).
[23] M.F. Zaeh, G. Branner, Investigations on residual stresses and deformations in selective laser melting, Prod. Eng. 4 (1) (2010) 35–45.
[24] P. Witherell, S. Feng, T.W. Simpson, D.B. Saint John, P. Michaleris, Z.-K. Liu, L.-Q. Chen, R. Martukanitz, Toward metamodels for composable and reusable additive manufacturing process models, J. Manuf. Sci. Eng. 136 (6) (2014) 061025.
[25] S. Clijsters, T. Craeghs, J.-P. Kruth, A priori process parameter adjustment for SLM process optimization, Innovative Developments on Virtual and Physical Prototyping, Taylor & Francis Group, 2012, pp. 553–560.
[26] H. Gong, K. Rafi, H. Gu, T. Starr, B. Stucker, Analysis of defect generation in Ti-6Al-4V parts made using powder bed fusion additive manufacturing processes, Addit. Manuf. 1 (2014) 87–98.
[27] F. Neugebauer, N. Keller, V. Ploshikhin, H. Koehler, Multi scale FEM simulation for distortion calculation in additive manufacturing of hardening stainless steel, International Workshop on Thermal Forming in welding distortion, IWOTE 14, Bremin, Germany, 2014.
[28] M. Langelaar, Topology optimization of 3D self-supporting structures for additive manufacturing, Addit. Manuf. 12 (2016) 60–70.
[29] K. Zeng, C. Teng, S. Xu, T. Sublette, N. Patil, D. Pal, B. Stucker, A comparison of the computational speed of 3DSIM versus ANSYS finite element analyses for simulation of thermal history in metal laser sintering, 25th Solid Freeform Fabrication Symposium, Austin, TX, USA, 2014.
[30] K. Zeng, D. Pal, H. Gong, N. Patil, B. Stucker, Comparison of 3DSIM thermal modelling of selective laser melting using new dynamic meshing method to ansys, Mater. Sci. Technol. 31 (8) (2015) 945–956.
[31] Y. Yang, M. Knol, F. van Keulen, C. Ayas, A semi-analytical thermal modelling approach for selective laser melting, Addit. Manuf. 21 (2018) 284–297.
[32] J. Heigel, P. Michaleris, E. Reutzel, Thermo-mechanical model development and validation of directed energy deposition additive manufacturing of Ti-6Al-4V, Addit. manufacturing 5 (2015) 9–19.
[33] T. Mukherjee, W. Zhang, T. DebRoy, An improved prediction of residual stresses and distortion in additive manufacturing, Comput. Mater. Sci. 126 (2017) 360–372.
[34] T. Mukherjee, H. Wei, A. De, T. DebRoy, Heat and fluid flow in additive manufacturing. Part I: Modeling of powder bed fusion, Comput. Mater. Sci. 150 (2018) 304–313.
[35] N. Keller, V. Ploshikhin, New method for fast predictions of residual stress and distortion of AM parts, 25th Solid Freeform Fabrication Symposium, Austin, TX, USA, 2014.
[36] C. Li, C. Fu, Y. Guo, F. Fang, Fast prediction and validation of part distortion in selective laser melting, Proc. Manuf. 1 (2015) 355–365.
[37] V. Ploshikhin, A. Prihodovsky, A. Ilin, C. Heimerdinger, Advanced numerical method for fast prediction of welding distortions of large aircraft structures, Int. J. Microstruct. Mater. Prop. 5 (4–5) (2010) 423–435.
[38] P. Alvarez, J. Ecenarro, I. Setien, M. San Sebastian, A. Echeverria, L. Eciolaza, Computationally efficient distortion prediction in powder bed fusion additive manufacturing, Int. J. Eng. Res. Sci. 2 (2016).
[39] M. San Sebastian, I. Setien, A.M. Mancisidor, A. Echeverria, SLM (near)-net-shape part design optimization based on numerical prediction of process induced distortions, TMS 2017 146th Annual Meeting & Exhibition Supplemental Proceedings, Springer, 2017, pp. 117–126.
[40] I. Setien, M. Chiumenti, S. van der Veen, M. San Sebastian, F. Garciandia, A. Echeverria, Empirical methodology to determine inherent strains in additive manufacturing, Comput. Math. Appl. Accepted (TBE), TBE (2018).
[41] G. Holzapfel, Nonlinear Solid Mechanics: A Continuum Approach for Engineering, John Wiley & Sons, Ltd., West Sussex, England, 2000.
[42] G. Dhondt, The Finite Element Method for Three-Dimensional Thermomechanical Applications, John Wiley & Sons, 2004.
[43] M. Smith, ABAQUS/Standard User's Manual, Version 6.9, (2009).
[44] J. CHEN, W. SHEN, Z. YIN, S. XIAO, Simulation of welding temperature distribution based on element birth and death, Hot Work. Technol. 7 (2005) 64–65.
[45] D. Flanagan, T. Belytschko, A uniform strain hexahedron and quadrilateral with orthogonal hourglass control, Int. J. Numer. Methods Eng. 17 (5) (1981) 679–706.
[46] Calculix Documentation, Version 2.12, Guido Dhondt and Klaus Wittig, 2017.